Modeling the Trade-Wind Cumulus Boundary Layer. Part II: A High-Order One-Dimensional Model

PH. BOUGEAULT

Direction de la Météorologie, EERM/GMD, 92100 Boulogne, France

(Manuscript received 20 January 1981; in final form 25 June 1981)

ABSTRACT

A numerical simulation of the trade-wind cumulus layer observed in the region of Puerto Rico is presented. The model is one-dimensional with a higher-order turbulence closure scheme (quasi-Gaussian assumption in the third-order moments equations). Conservative variables are used, and the clouds are parameterized according to the propositions of Part I of this paper, using a skewed exponential scheme. Once a quasi-steady state has been reached in the simulation, the results of the model are compared with satisfactory agreement to statistics on the data of a detailed three-dimensional cloud model. The one-dimensional model proves to be able to compute with reasonable accuracy the profiles of all turbulent quantities up to third-order moments. It therefore is suggested that this kind of model can provide valuable results in cloudy planetary boundary layer studies.

1. Introduction

In the first part of this paper (Bougeault, 1981, hereafter referred to as Part I), problems relative to the numerical modeling of turbulent planetary boundary layers (PBL) including a condensation cycle have been considered. As already suggested by Betts (1973), Deardorff (1976), Sommeria and Deardorff (1977), Mellor (1977), Yamada and Mellor (1979), it has been shown that conservative variables θ_l and q_w can be conveniently used, as far as warm clouds with no supersaturation are concerned. However, the approach leads to a specific closure problem: the liquid water specific content q_l appears in the virtual potential temperature, so that all the buoyancy production terms involve correlations with this unknown liquid water content. All these quantities therefore must be parameterized from an adequate subgrid condensation scheme. Such schemes rely on a probability density assumption for the vertical velocity w and for a linear combination of the main variables, which controls the condensation processes. An efficient law was found by analyzing the results of Sommeria's (1976) three-dimensional (3D) numerical trade-wind cumulus model.

In this Part II, we propose a third-order one-dimensional (1D) model for the simulation of the cloudy PBL, derived from the model described by André *et al.* (1976a,b; 1978). It includes the parameterizations derived in Part I and a few other modifications. In order to test this model, we present results from a very short simulation, starting from the initial mean profiles of the Puerto Rico experiment (Sommeria and LeMone, 1978), with all turbulent quantities (i.e., double and triple correlations) set to zero. After a few hours of simulated time, the model produces realistic values for these quantities. These results are analyzed and compared to those of Sommeria's model. Both models have equivalent theoretical limitations, and are found to be in good agreement with each other, with the one exception that the 1D model cannot easily deal with the large values of the third-order moments without leading to numerical instability. This is not very surprising, since this model is based on the quasi-Gaussian assumption for the fourth-order moments, which is not very consistent with the large skewness and flatness factors encountered in the cloud layer. Nevertheless, results are quite satisfactory, at least as far as second moments are concerned.

Condensation and radiative processes can strongly interact in clouds, by cooling the upper parts and warming the lower parts, leading to further destabilization. Despite this fact, no attempt is made here to include a detailed description of this interaction, and a constant radiative cooling rate $\bar{R}$ is introduced in the model. The reason is that this paper aims to focus on the description of the dynamics–condensation interaction, but the model is general enough to be modified whenever detailed radiative calculations are needed. On the other hand, and though it is well-known that radiation can drive the evolution of stratus, stratocumulus or fog (Lilly, 1968; Oliver *et al.*, 1978; Manton, 1979; Randall, 1980), attempts have been made only recently to investigate the short-term effects of radiation on the development of cumulus cloud layers (see Veyre *et al.*, 1980).

0022-4928/81/112429-11$06.75

2. Description of the model

As stated in Part I, we use the three components of the velocity, u, v, w and the conservative liquid water potential temperature θ_l, and total water specific content q_w as prognostic variables. According to the Boussinesq approximation, equations are written for the fluctuations from an isentropic and hydrostatic reference state. The turbulence equations for the statistical moments of the prognostic variables are then derived up to third-order correlations, with adequate closure assumptions. Following André *et al.* (1978), we assume that dissipative scales are isotropic for modeling molecular destruction. We neglect molecular diffusive fluxes, and model the pressure correlations as the sum of a return-to-isotropy term and a rapid term (Launder, 1975). We further use a single time scale τ for all closure assumptions, designed as the time scale of the largest eddies or clouds, and dimensionally related to the turbulence kinetic energy by use of a prescribed energetic length scale. Let ϵ be the dissipation of the turbulence kinetic energy $\bar{e}$. It is then assumed that $\tau = \bar{e}/\epsilon$, with $\epsilon = \bar{e}^{3/2}/\mathsf{L}(z)$, where $\mathsf{L}(z)$ is derived from Blackadar's (1962) length inside the mixed layer, i.e., $\mathsf{L}(z) = C_1^{-1}kz/(1 + kz/L_\infty)$. The von Kármán constant k was taken as 0.35, the constant C_1 was given its usual value of 0.07 (André *et al.*, 1978), and L_∞ was adjusted as 15% of the mixed-layer depth. Inside the cloud layer, $\mathsf{L}(z)$ was given a constant value L_C equal to 250 m, which is consistent with the observed size of clouds in the 3D model. The resulting profile of $\mathsf{L}(z)$ can be seen in Fig. 1. The results discussed in Section 5 are not very sensitive to the values of L_∞ and L_C. Coriolis effects have been neglected, except in the first-order moment equations. The fourth-order moments are expressed by use of the quasi-Gaussian approximation:

$$\overline{a'b'c'd'} = \overline{a'b'}\cdot\overline{c'd'} + \overline{a'c'}\cdot\overline{b'd'} + \overline{a'd'}\cdot\overline{b'c'}.$$

The final set therefore contains 50 equations, which can be written in the following way, using the symbolic form u_i for u, v, w and a, b, for θ_l, q_w:

1) The prognostic equations for the four mean quantities are:

$$\frac{\partial \bar{u}}{\partial t} = -\frac{\partial}{\partial z}\overline{w'u'} + f(\bar{v} - v_g) - \bar{w}\frac{\partial \bar{u}}{\partial z}, \tag{1a}$$

$$\frac{\partial \bar{v}}{\partial t} = -\frac{\partial}{\partial z}\overline{w'v'} - f(\bar{u} - u_g) - \bar{w}\frac{\partial \bar{v}}{\partial z}, \tag{1b}$$

$$\frac{\partial \overline{\theta_l}}{\partial t} = -\frac{\partial}{\partial z}\overline{w'\theta_l'} - \bar{w}\frac{\partial \overline{\theta_l}}{\partial z} - \bar{R}, \tag{1c}$$

$$\frac{\partial \overline{q_w}}{\partial t} = -\frac{\partial}{\partial z}\overline{w'q_w'} - \bar{w}\frac{\partial \overline{q_w}}{\partial z}. \tag{1d}$$

The Coriolis parameter f is given a value of 4.75 $\times$ 10^{-5} s^{-1}, and the radiative cooling rate $\bar{R}$ is taken as 1.5 $\times$ 10^{-5} K s^{-1} throughout the layer. According to Sommeria and LeMone, this value is necessary to balance the warming by surface heat flux. The large-scale subsidence $\bar{w}(z)$ and the horizontal components of the geostrophic wind u_g, v_g are prescribed and constant during the simulation. Their profiles are shown in Fig. 1.

2) The tendencies of the six velocity correlations $\overline{u'^2}$, $\overline{v'^2}$, $\overline{w'^2}$, $\overline{u'v'}$, $\overline{v'w'}$, $\overline{u'w'}$, are

$$\begin{aligned}\frac{\partial}{\partial t}\overline{u_i'u_j'} &= -\frac{\partial}{\partial z}\overline{w'u_i'u_j'}\\ &\quad - (1 - C_5)\left\{\overline{u_i'w'}\frac{\partial \bar{u}_j}{\partial z} + u_j'w'\frac{\partial \bar{u}_i}{\partial z}\right.\\ &\quad \left. - \beta\overline{u_i'\theta_v'}\delta_{3j} - \beta\overline{u_j'\theta_v'\delta_{3i}}\right\} - \tfrac{2}{3}\epsilon\delta_{ij}\\ &\quad - \frac{C_4}{\tau}(\overline{u_i'u_j'} - \tfrac{2}{3}\delta_{ij}\bar{e})\\ &\quad + C_5\tfrac{2}{3}\delta_{ij}\left\{\beta\overline{w'\theta_v'} - \overline{u'w'}\frac{\partial \bar{u}}{\partial z} - \overline{v'w'}\frac{\partial \bar{v}}{\partial z}\right\},\end{aligned} \tag{2}$$

where β is the buoyancy coefficient.

3) The tendencies of the three scalar correlations $\overline{\theta_l'^2}$, $\overline{q_w'^2}$, $\overline{\theta_l'q_w'}$, are

$$\begin{aligned}\frac{\partial}{\partial t}\overline{a'b'} &= -\frac{\partial}{\partial z}\overline{w'a'b'} - \left\{\overline{a'w'}\frac{\partial \bar{b}}{\partial z} + \overline{b'w'}\frac{\partial \bar{a}}{\partial z}\right\}\\ &\quad - \frac{C_2}{\tau}\overline{a'b'}.\end{aligned} \tag{3}$$

4) The tendencies of the six fluxes of scalar quantities $\overline{w'\theta_l'}$, $\overline{w'q_w'}$, $\overline{u'\theta_l'}$, $\overline{u'q_w'}$, $\overline{v'\theta_l'}$, $\overline{v'q_w'}$, are

$$\begin{aligned}\frac{\partial}{\partial t}\overline{u_i'a'} &= -\frac{\partial}{\partial z}\overline{w'u_i'a'} - \overline{u_i'w'}\frac{\partial \bar{a}}{\partial z} - (1 - C_7)\\ &\quad \times \left\{\overline{w'a'}\frac{\partial \bar{u}_i}{\partial z} - \beta\delta_{3i}\overline{\theta_v'a'}\right\} - \frac{C_6}{\tau}\overline{u_i'a'}.\end{aligned} \tag{4}$$

5) The tendencies of the six fluxes of velocity correlations $\overline{w'u'^2}$, $\overline{w'v'^2}$, $\overline{w'^3}$, $\overline{w'u'v'}$, $\overline{w'v'w'}$, $\overline{w'u'w'}$, are

$$\begin{aligned}\frac{\partial}{\partial t}\overline{u_i'u_j'w'} &= -\overline{u_i'w'}\quad\frac{\partial u_j'w'}{\partial z} - \overline{u_j'w'}\frac{\partial \overline{u_i'w'}}{\partial z}\\ &\quad - \overline{w'^2}\frac{\partial \overline{u_i'u_j'}}{\partial z} + \left\{\beta\overline{u_i'u_j'\theta_v'} + \beta\delta_{3j}\overline{u_i'w'\theta_v'}\right.\\ &\quad \left. + \beta\delta_{3i}\overline{u_j'w'\theta_v'} - \overline{u_i'w'^2}\frac{\partial \overline{u_j}}{\partial z} - \overline{u_j'w'^2}\frac{\partial \overline{u_i}}{\partial z}\right\}\\ &\quad \times (1 - C_{11}) - \frac{C_8}{\tau}\overline{u_i'u_j'w'}.\end{aligned} \tag{5}$$

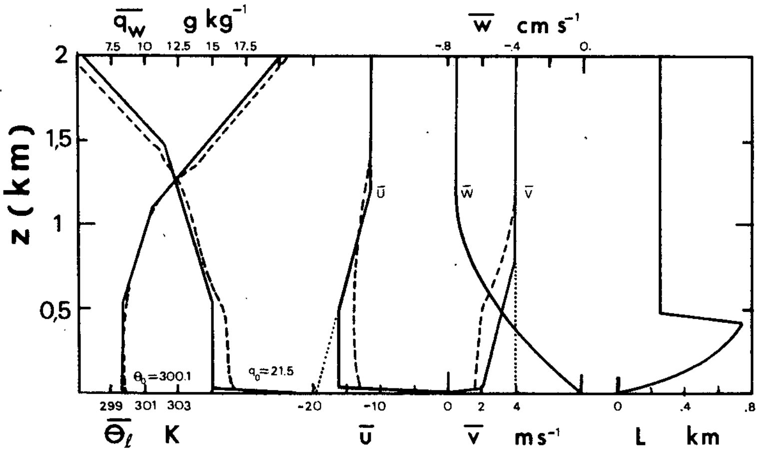

FIG. 1. Profiles of the mean variables at $t = 0.0$ (solid lines) and at $t = 2.5$ (dashed lines). The geostrophic wind (dotted lines), the vertical velocity w and the mixing length L are constant during the experiment.

6) The tendencies for the four third-order scalar correlations $\overline{\theta_l'^3}$, $\overline{\theta_l'^2 q_w'}$, $\overline{\theta_l' q_w'^2}$, $\overline{q_w'^3}$, are

$$\frac{\partial}{\partial t}\overline{a'^2b'} = -\overline{w'b'}\,\frac{\partial\overline{a'^2}}{\partial z} - 2\overline{w'a'}\,\frac{\partial\overline{a'b'}}{\partial z} - \overline{w'a'^2}\,\frac{\partial\bar{b}}{\partial z} - 2\overline{w'a'b'}\,\frac{\partial\bar{a}}{\partial z} - \frac{C_{10}}{\tau}\,\overline{a'^2b'}. \quad (6)$$

7) The tendencies for the twelve "fluxes of fluxes" $\overline{u'^2\theta_l'}$, $\overline{u'v'\theta_l'}$, $\overline{u'w'\theta_l'}$, $\overline{v'^2\theta_l'}$, $\overline{v'w'\theta_l'}$, $\overline{w'^2\theta_l'}$, $\overline{w'^2q_w'}$, $\overline{u'^2q_w'}$, $\overline{u'v'q_w'}$, $\overline{u'w'q_w'}$, $\overline{v'^2q_w'}$, $\overline{v'w'q_w'}$, are

$$\frac{\partial}{\partial t}\overline{u_i'u_j'a'} = -\overline{w'a'}\,\frac{\partial\overline{u_i'u_j'}}{\partial z} - \overline{u_i'w'}\,\frac{\partial\overline{u_j'a'}}{\partial z} - u_j'w'\,\frac{\partial\overline{u_i'a'}}{\partial z} - \overline{u_i'u_j'w'}\,\frac{\partial\bar{a}}{\partial z} + \left\{\beta\overline{u_i'a'\theta_v'}\delta_{3j} + \beta\overline{u_j'a'\theta_v'}\delta_{3i} - \overline{u_i'w'a'}\,\frac{\partial\overline{u_j}}{\partial z} - \overline{u_j'w'a'}\,\frac{\partial\overline{u_i}}{\partial z}\right\}(1 - C_{11}) - \frac{C_8}{\tau}\,\overline{u_i'u_j'a'}. \quad (7)$$

8) Finally, the tendencies for the nine fluxes of scalar correlations $\overline{u'\theta_l'^2}$, $\overline{v'\theta_l'^2}$, $\overline{w'\theta_l'^2}$, $\overline{u'q_w'^2}$, $\overline{v'q_w'^2}$, $\overline{w'q_w'^2}$, $\overline{u'\theta_l'q_w'}$, $\overline{v'\theta_l'q_w'}$, $\overline{w'\theta_l'q_w'}$, are

$$\frac{\partial}{\partial t}\overline{u_i'a'b'} = -\overline{u_i'w'}\,\frac{\partial\overline{a'b'}}{\partial z} - \overline{w'a'}\,\frac{\partial\overline{u_i'b'}}{\partial z} - \overline{w'b'}\,\frac{\partial\overline{u_i'a'}}{\partial z} - \overline{u_i'w'a'}\,\frac{\partial\bar{b}}{\partial z} - \overline{u_i'w'b'}\,\frac{\partial\bar{a}}{\partial z} + \left\{\beta\overline{\theta_v'a'b'}\delta_{3i} - \overline{w'a'b'}\,\frac{\partial\overline{u_i}}{\partial t}\right\}(1 - C_{11}) - \frac{C_8}{\tau}\,\overline{u_i'a'b'}. \quad (8)$$

The set of constants used in these equations has been determined from previous experiments (André *et al.*, 1976a,b), with the following exceptions. The constant C_2 needed further adjustment and was taken as 1.3, instead of the previously used 2.5. Its magnitude is now in good agreement with the values used by most authors (e.g., Wyngaard and Coté, 1974; Launder, 1975). In the first experiments, instability appeared whenever the third-order moments had large values. As in André *et al.* (1978), this early model used a "clipping" approximation to damp the growth of the third-order moments. Namely, they were cut off whenever they exceeded the maximum permissible value according to the quasi-Gaussian assumption. Clearly, this cut-off is not consistent with the large flatness factors observed in the cloud layer (see Part I, and Section 5 of this paper), and is due to the extreme values linked to strong upward motions. It was suspected to be the reason for instability. As an attempt to remedy the problem, clipping was no longer used, and a "rapid" term was introduced in the parameterization of the pressure term in the third-order moment equations. It was taken proportional to the production term arising from the velocity fluctuation equation, with an adjustable numerical coefficient C_{11}. Another approach has been developed by André *et al.* (1981), where the same term is modeled as proportional to the anisotropic part of the production tensor, the difference being effective for the equation in $\overline{u_i'u_j'a'}$ only. We experienced different values of C_{11}, with the only result that large values of the third-order moments lead almost systematically to instability. So in the cloud layer these moments had to be kept to smaller values than those of their 3D counterparts, as can be seen in Section 5. This was obtained by choosing a somewhat larger value of C_{11} (0.4, as compared to 0.2 in André *et al.*, 1981), and accordingly a smaller value of C_8 (6.5, as compared to 8). Other numerical refinements were included in the model, but did not lead to any improvement in the results. A conclusion therefore is that a possible lack of consistency between the quasi-Gaussian assumption and the non-Gaussian cloud parameterization may be responsible for this instability, rather than the enforcement of realizability through clipping. The quasi-Gaussian assumption may then have to be given up in such a case, and a convenient way could be to add a diffusion term according to the proposition of Deardorff (1978). Another possible explanation is that the cloud parameterization is derived from an empirical assumption of maximum correlation between all variables inside the cloud layer [see Part I, Eq. (8)]. This could lead to a positive feedback between second and third-order moments. The parameterization may then have to be improved by introducing some correlation coefficient, less than unity, estimated from the correlation coefficient between conservative variables. The following set of constants was finally used: $C_2 = 1.3$, $C_4 = 4.5$, $C_5 = 0$, $C_6 = 4.85$, $C_7 = 0.4$, $C_8 = 6.5$, $C_{10} = 3C_2$ and $C_{11} = 0.4$.

Whenever the virtual potential temperature θ_v appears in Eqs. (1)–(8), it is expressed as described in Part I, following:

$$\theta_v' = \theta_l' + 0.61T_0 q_w' + \left[\left(\frac{p_0}{p_r(z)}\right)^k \frac{L}{C_p} - 1.61T_0\right] q_l', \quad (9)$$

where T_0 is a mean value of the absolute temperature, taken as 300 K, L the latent heat of condensation of water, C_p the specific heat for moist air, p_0 the reference pressure 10^5 Pa, and $p_r(z)$ the mean pressure of the Boussinesq reference atmosphere at height z. The correlations including the liquid water content, arising from the buoyancy terms $\beta\overline{m'\theta_v'}$, $\beta\overline{m'n'\theta_v'}$, are parameterized as described in Part I. Let us define

$$q_{sl} = q_s[\theta_l, p_r(z)],$$

$$a = [1 + (L^2/R_v C_p \overline{T_l}^2) q_{sl}]^{-1},$$

$$\alpha_1 = \overline{q_{sl}}(L/R_v \bar{T}_l^2)\{[p_r(z)]/p_0\}^k,$$

$$\sigma_s = \frac{a}{2}(\overline{q_w'^2} + \alpha_1^2 \overline{\theta_l'^2} - 2\alpha_1 \overline{q_w'\theta_l'})^{1/2},$$

$$Q_1 = a(\overline{q_w} - \overline{q_{sl}})/2\sigma_s.$$

It is assumed that, for m, n, being any θ_l, q_w, u_i

$$\overline{q_l} = 2\sigma_s \exp(Q_1 - 1), \quad (10a)$$

$$\overline{m'q_l'} = 2\sigma_m\sigma_s(2 - Q_1)\exp(Q_1 - 1), \quad (10b)$$

$$\overline{m'n'q_l'} = 2\sigma_m\sigma_n\sigma_s(Q_1^2 - 4Q_1 + 5) \times \exp(Q_1 - 1), \quad (10c)$$

where σ_m is $(\overline{m'^2})^{1/2}$ and $Q_1 \leqslant 1$ for the case studied.

3. The Puerto Rico Experiment: Definition and mean profiles

The PBL, as observed during the Puerto Rico Experiment (Pennell and LeMone, 1974; LeMone and Pennell, 1976), shows a three-layer structure. A convectively mixed layer is topped by a stable layer where cumulus clouds can develop by conditional instability of the first kind. The mean cloud top level coincides with the trade inversion. Above this level, the stratification is stable, and the only possible movements are internal waves. The humidity decreases linearly in the two upper layers. A 3 h numerical experiment is performed using these initial conditions. Fig. 1 shows the mean profiles of $\bar{u}$, $\bar{v}$, $\overline{\theta_l}$, $\overline{q_w}$, at $t = 0.00$ (beginning of the run) and $t = 2.50$ h, along with the prescribed $\bar{w}(z)$, L(z). These profiles have been taken from the 3D simulation by Sommeria and LeMone (1978). The surface values of $\overline{\theta_l}$ and $\overline{q_w}$ are assumed constant during the run. At $t = 0.00$ all turbulence quantities are set to zero, which, considering the absence of any relevant data, amounts to the simplest possible choice. Convection develops in both 1D and 3D models under the forcing of the surface fluxes, computed from the same flux-profile relationships at the first level (25 m above the surface), i.e., the formulation of Businger *et al.* (1971). This leads to a regular but slow decrease of the surface fluxes during the run, from 1.2×10^{-4} to 0.9×10^{-4} m s^{-1} kg kg^{-1} for $(\overline{w'q_w'})_s$, and from 6×10^{-3} to 3.5×10^{-3} m K s^{-1} for $(\overline{w'\theta_l'})_s$.

Clouds do appear after 0.5 h, as a consequence of increasing humidity, and temperature and moisture fluctuations, and develop to reach a maximum. After roughly 2 h of simulated time, the turbulence moments reach a quasi-steady state, and evolve then much more slowly. Fig. 2 shows the evolution of the cloud activity during the 1D and 3D runs. We have chosen $\overline{q_l}_{\max}$, the largest value of the liquid water mean content with respect to altitude, as an indicator. Clearly, the 1D model smoothes out the short-term fluctuations linked to the development of individual clouds in the 3D model. It further underestimates slightly the liquid water content, but the location and depth of the cloud layer are well predicted, as can also be seen in Fig. 8. The lower limit of the cloud layer mainly depends on the pressure variation with height, which is taken into account through the expression of $\overline{q_{sl}}$. The upper limit is determined by a balance between the vertical turbulent flux of moisture and the drying effect of subsidence.

Returning to Fig. 1, we can see that the convection leads to an increase of moisture in the whole layer, and that at $t = 2.50$, the profile of $\overline{q_w}$ shows a characteristic gradient in the mixed layer (André *et al.*, 1979). On the contrary, the time rate of change of $\overline{\theta_l}$ is very small, since the radiative cooling balances

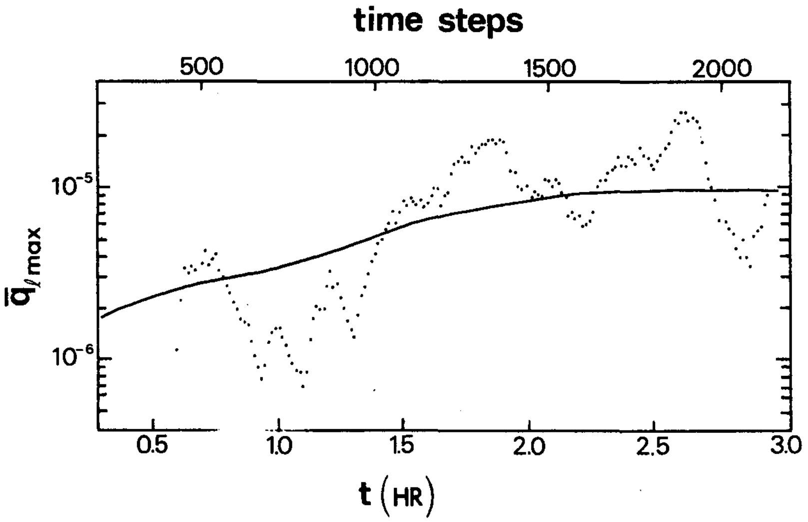

FIG. 2. Evolution of the maximum of the mean liquid water content with respect to the altitude, both in the 3D run (points) and in the 1D run (solid line).

mainly the turbulent heating. The long-term evolution is linked with this evolution of the mean profiles, which would interact with the diurnal cycle in the real atmosphere. As noted earlier, our model does not presently take into account this long-term evolution (e.g., through detailed radiative computations, and evolution of the surface parameters). It therefore is only possible to focus on the turbulent moments, once a quasi-equilibrium has been reached. We shall study these quantities by comparing the 1D results to the 3D data.

4. A comparison of 1D and 3D results

Testing results of a sophisticated turbulence model against experimental data raises a huge problem, as soon as quantitative results are needed. This validation is however absolutely necessary, especially in the case of a 1D model, because of the numerous closure assumptions involved. For the past 10 years, aircraft measurements have been successfully taken inside the mixed layer, allowing for an analysis of the variances, fluxes, and budgets of the main quantities (e.g., Lenschow, 1970; Wyngaard *et al.*, 1978). To our knowledge, detailed turbulence measurements inside cloud layers (including measurements in the clouds themselves) have not yet been published.

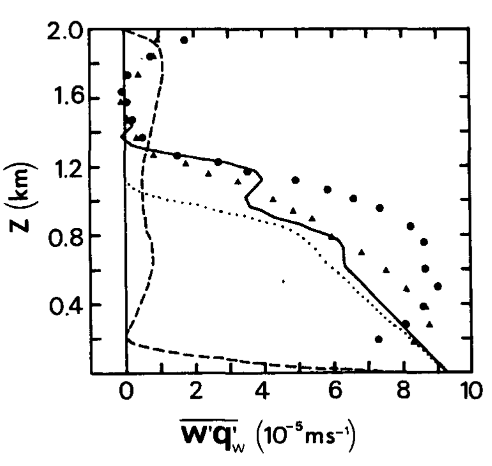

FIG. 3. Flux of total water content. Solid line: 1D result at t = 2.5 h; dotted line: 1D result with Gaussian cloud scheme; triangles: 3D results averaged from 2.28 to 2.54 h; circles: 3D results averaged from 2.42 to 2.68 h; dashed lines: subgrid-scale contribution in the 3D results.

Using data generated by a 3D detailed turbulence model seems therefore a very attractive alternative method, since it may be presumed that such a model deals effectively with the turbulence movements, depends only weakly on the unavoidable closure assumptions, and provides as many data as needed. As stated in Part I, we have computed statistical second- and third-order moments of the distribution

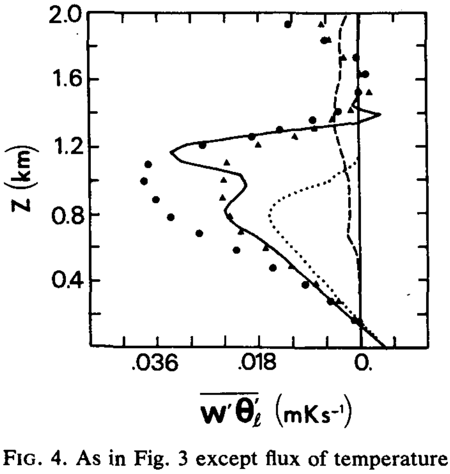

FIG. 4. As in Fig. 3 except flux of temperature.

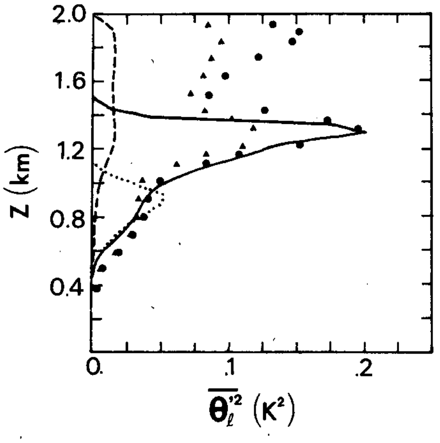

FIG. 5. As in Fig. 3 except variance of temperature.

of the main variables in horizontal planes with which to compare the profiles of these quantities with the results of the 1D model, plotted in Figs. 3–21. For comparison, we also have plotted results of a 1D run using the Gaussian cloud parameterization instead of Eqs. (10) (see Part I). Of course, any model has shortcomings that must be carefully examined. The 3D model used in this study has been described by Sommeria (1976) and attention must be given to the following main limitations:

1) *Lack of ergodicity*: For all the computations to be reported, as for deriving the 1D model equations, we approximate the ensemble means as averages in time and over horizontal planes. As the time scales of turbulent eddies and of evolution of the mean profiles may not be very different, this is a serious limitation to the accuracy of the results. Nevertheless, the errors should not exceed an order of magnitude, if the averaging time is carefully chosen. It should be noted that the same problem arises when analyzing aircraft turbulence data. In order to give better insight into this problem, two sets of symbols have been plotted on the figures, corresponding to averages of 3D data computed from two slightly shifted time series of 1000 seconds (2.28 to 2.54 h and 2.42 to 2.68 h).

2) *Lack of small-scale description*: In order to overcome this shortcoming, the grid size is chosen small enough to be within the generally accepted scale of the turbulence inertial range (here 50 m). The subgrid fluxes are parameterized from an eddy diffusion scheme, which takes into account the effects of stability. The amount of subgrid condensation is computed according to the Gaussian assumption, as stated by Sommeria and Deardorff (1977). In Part I, we have pointed out that the overall result is not very sensitive to the assumed subgrid distribution of the variables. Whenever it was possible, that is, for the double correlations, the subgrid-scale fractions of the considered moments have been plotted (Fig. 3–7 and 12), according to their parameterization used in the 3D model. Except near the surface, they do not exceed 10% of the total value computed from the grid points values, i.e., less than the sampling error.

3) *Lack of mesoscale description*: The integration domain for the 3D model is a (2 km)^3 cube, with cyclic lateral boundary conditions. Consequently, the model cannot deal with larger mesoscale patterns, such as cellular convection, or cloud streets, which could affect significantly the distribution of the variables as well as the cloud statistics. The only remedy would be to increase the integration domain, leading to an increase in computing time and memory use, since the grid size has to be kept inside the inertial range. On the other hand, for the case studied here, the mean horizontal diameter of the clouds is roughly 200 m and a possible gap could exist between mesoscales and cloud scales, allowing for a parameterization of the interactions. Nonetheless, this is the main shortcoming of such a model, but it should be noticed that the 1D model has exactly the same limitations.

4) *Upper and lower boundary conditions*: At the lower boundary, small-scale (subgrid) fluxes are prescribed according to the Monin-Obukhov similarity theory, and velocity is set to zero, so that when height increases, subgrid fluxes are progressively relieved by the resolvable scale fluxes, leading to difficulties in estimating the moments. This region is not considered in the figures. At the upper boundary, vertical velocity is set to zero, which seems to be convenient, unless strong internal gravity waves are present in the stable layer. The wavenumbers of these possible internal waves are selected by the model according to the cyclic lateral boundary conditions, and their spectrum therefore is unrealistic. However, the study of the interaction of these "model waves" with the turbulence could still be of interest.

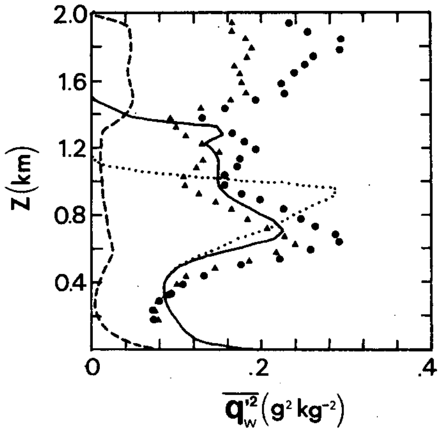

FIG. 6. As in Fig. 3 except variance of humidity.

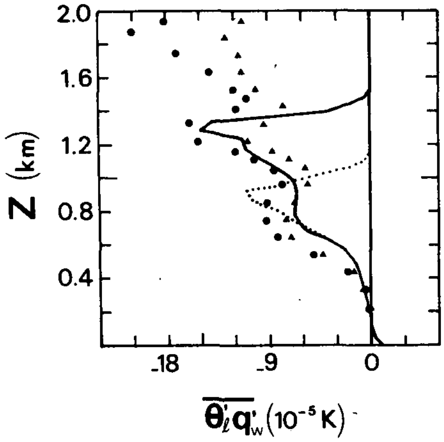

FIG. 7. As in Fig. 3 except covariance of temperature and humidity.

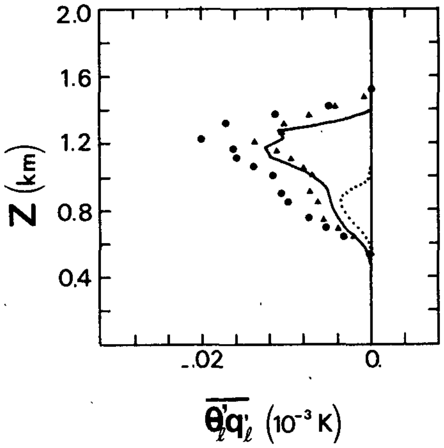

FIG. 9. As in Fig. 3 except covariance of temperature and liquid water content.

5) *Anomalous results near the inversion*: Many authors have noted anomalous results near the inversion (Deardorff, 1974; Wyngaard and Coté, 1974; André *et al.*, 1978), namely, the presence of spurious negative humidity fluxes just above the inversion, where humidity decreases rapidly with height. In the absence of any negative source, the flux should be positive in this region. Although this feature may appear instantaneously in field experiment data, L. Nahrt, private communication), it is not likely to persist when the flux is averaged over 15 min. The models therefore are in error in this region, and until now, no convincing explanation has been proposed. Interestingly, this problem appears in both 1D and 3D models.

5. The profiles of the turbulent correlations

It can be checked from the figures that the 1D model provides a good overall agreement with the 3D calculations, whereas the use of the Gaussian scheme leads to the underestimation of the turbulent quantities inside the cloud layer, as well as of the cloud-layer depth.

The flux of total water content is shown in Fig. 3. If one accepts the spurious oscillations in the 1D result, it decreases throughout the mixed and cloud layers. Clearly, the main source for the flux is the evaporation at the surface, leading to the observed increase of moisture in the whole layer. This feature is not likely to be universal. Results of field experiments have shown that the moisture flux can show a maximum near the inversion layer, leading to the drying of the mixed layer. Similarly, Sommeria (1976) has published results where the flux is maximum inside the cloud layer. Nonetheless, this profile is not linear, and moisture increases more rapidly in the cloud layer than in the mixed layer.

The flux of temperature $\overline{w'\theta_l'}$ shows also spurious oscillations (Fig. 4). It is almost linear throughout the layer in the 3D data. Inside the mixed layer, q_l is zero, and θ_l reverts to θ. The linearity is therefore a well-known feature. Near the surface, the flux is positive, because the updrafts carry warm air from

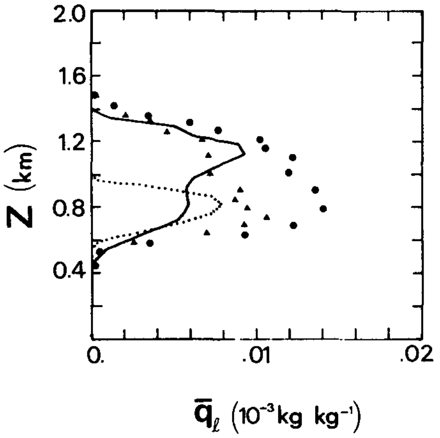

FIG. 8. As in Fig. 3 except mean liquid water content.

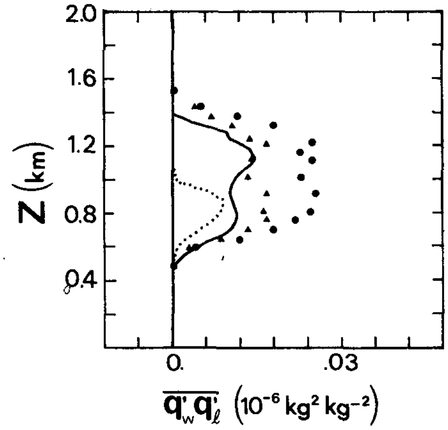

FIG. 10. As in Fig. 3 except covariance of liquid and total water content.

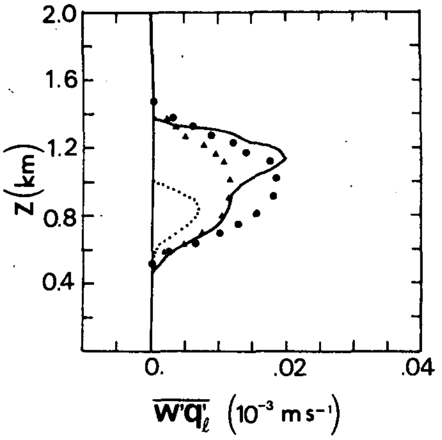

FIG. 11. As in Fig. 3 except vertical eddy flux of liquid water.

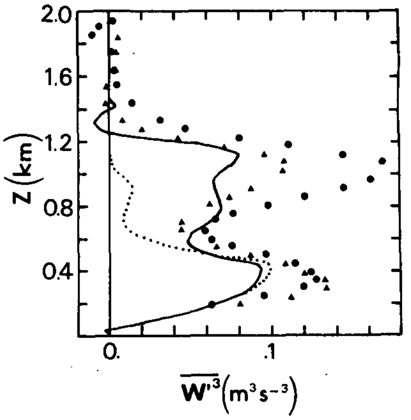

FIG. 13. As in Fig. 3 except vertical turbulent flux of the vertical velocity variance.

the lower levels. At ~100 m, the flux changes sign, and the updrafts carry relatively colder air, while temperature increases with height. Consequently, buoyant ascent is maintained by water vapor alone. Inside the cloud layer, the negative flux of θ_l accounts for the upward transport of q_l (let us remember that $\theta_l = \theta - (L/C_p)(\bar{\theta}/\bar{T})q_l$). As pointed out by Betts (1973), this flux shows a minimum inside the cloud layer, whose lower part is warmed by condensation, whereas the upper part is cooled by evaporation.

Fig. 5 shows the profile of the variance of temperature $\overline{\theta_l'^2}$. The scale of the figure prevents seeing the usual maximum near the surface, which is indeed present. Although θ_l is conservative, the variance is very large inside the cloud layer, because clouds induce strong updrafts in a stratified environment. The maximum occurs around the trade inversion level, where the gradient of θ_l is the largest (see Fig. 1). In the upper stable layer, the 1D result strongly departs from the 3D data, which show a secondary maximum. This is due to internal waves, which develop in the stable layer. As can be seen from Figs. 3 and 4, these movements are not associated with turbulent fluxes of θ_l and q_w (except for the subgrid-scale contribution). The corresponding values of the third-order moments also are very small (see Figs. 13–21), and we shall ignore these waves in this study.

The moisture variance $\overline{q_w'^2}$ is shown in Fig. 6. The above remarks also apply, but the surface value is here of greater importance. The maximum again occurs inside the cloud layer, while the mixed layer corresponds to relatively smaller values. The covariance $\overline{\theta_l' q_w'}$ (Fig. 7) also exhibits two maxima at the cloud base and at the trade inversion, which can be traced as being the main sources of inhomogeneities. It is positive near the surface, where rising parcels are warm and moist, and changes sign at the same height as $\overline{w'\theta_l'}$.

The next figure (Fig. 8) illustrates the parameterized mean liquid water content. The parameteriza-

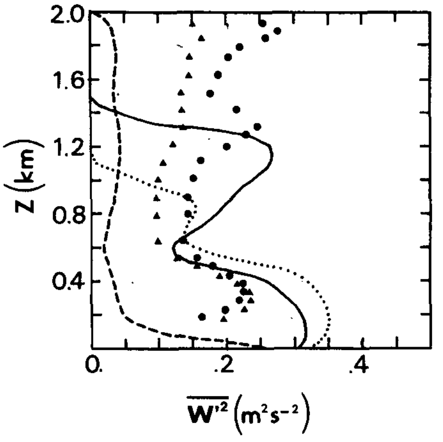

FIG. 12. As in Fig. 3 except vertical component of the turbulent kinetic energy.

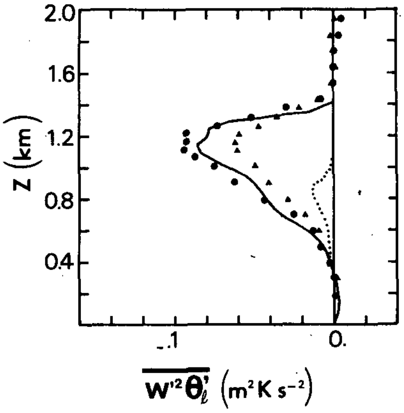

FIG. 14. As in Fig. 3 except vertical turbulent transport of temperature flux.

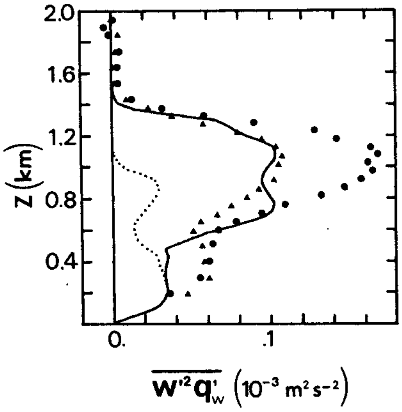

FIG. 15. As in Fig. 3 except vertical turbulent transport of the moisture flux.

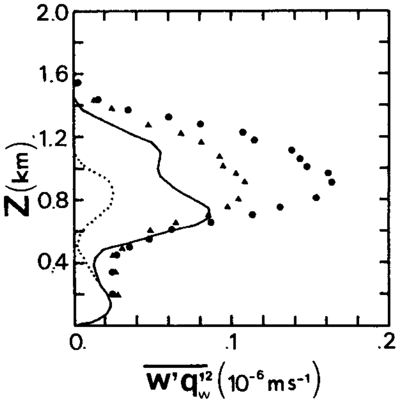

FIG. 17. As in Fig. 3 except the flux of humidity variance.

tion [Eq. (10)] slightly underestimates the mean liquid water content and correlations involving its fluctuations, as noted in Part I. Here the discrepancy with the 3D data is found to be as large as a factor of 2 in the lower part of the cloud layer. This is likely to be a consequence of the parameterizations for the second- and third-order moments, based on the skewed exponential scheme throughout the whole cloud layer. As noted in Part I, the lower levels are characterized by an almost Gaussian distribution of the variables. Therefore, Eqs. (10) will induce an overestimation of the upward transport. On the other hand, the Gaussian parameterization, which underestimates the transport, as can be seen from any other figure, leads locally to an artificially better value of $\overline{q_l}$. This is due to the overestimation of q_w, which arises from an underestimated growth rate of the cloud layer. This was in fact the main reason which led us to look for some new condensation scheme. A further improvement would be to use a scheme with variable skewness.

The same remarks apply for the liquid water correlations $\overline{\theta_l' q_l'}$ (Fig. 9), $\overline{q_w' q_l'}$ (Fig. 10), and $\overline{w' q_l'}$ (Fig. 11). The 3D data show two slight maxima inside the cloud layer for $\overline{\theta_l' q_l'}$ and $\overline{q_w' q_l'}$, which can be identified as two maxima of cloud activity. On the other hand, the flux $\overline{w' q_l'}$ exhibits a very regular shape with only one maximum, proving that the cloud layer as a whole is transferring moisture upward.

The vertical component of the turbulence kinetic energy ($\overline{w'^2}$, Fig. 12) shows two maxima. The lower one is a well-known feature of convective mixed layers. The other maximum, at the top of the cloud layer, is overestimated by the 1D model. It is produced by the buoyant acceleration of the parcels, when latent heat is released in the lower part of the cloud layer. The minimum near the cloud base is an interesting feature, proving that the rising parcels are slowed down by the stability effects, before condensation occurs.

The flux of $\overline{w'^2}$, i.e., $\overline{w'^3}$, is shown in Fig. 13. This flux is directed upward throughout the layer, and shows again distinct maxima inside the mixed and cloud layers, with a minimum at cloud base. It therefore is very similar to the $\overline{w'^2}$ profile, and it is not likely that any simple closure model for $\overline{w'^3}$ would

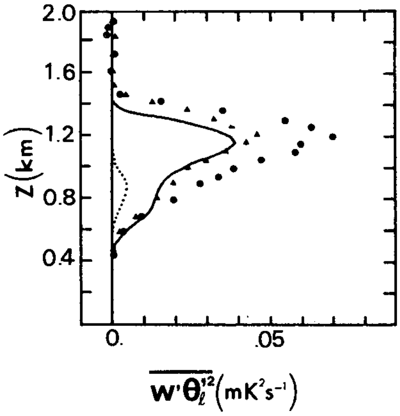

FIG. 16. As in Fig. 3 except the flux of temperature variance.

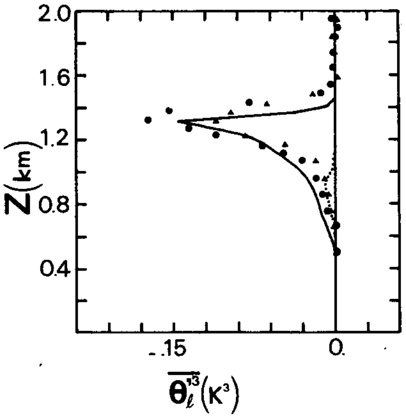

FIG. 18. As in Fig. 3 except the third-order moment of temperature.

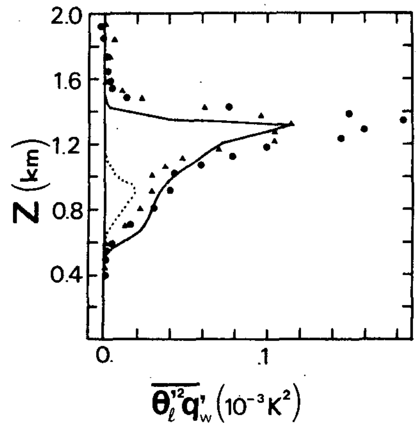

FIG. 19. As in Fig. 3 except the third-order correlation $\overline{\theta_l'^2 q_w'}$.

reproduce such a behavior. Our third-order 1D model provides the right sign and order of magnitude, as for all other third-order moments (see below). Unfortunately, the spurious oscillations already mentioned appear here also (see, e.g., Fig. 13), and damage the value of some third-order moments inside the cloud layer.

Figs. 14 and 15 show the "fluxes of fluxes" $\overline{w'^2\theta_l'}$ and $\overline{w'^2 q_w'}$. The agreement between the 1D and 3D results is satisfactory enough, although better for $\overline{w'^2\theta_l'}$ than for $\overline{w'^2 q_w'}$. Again, these fluxes have the same sign as the quantities they are transferring (see Figs. 3 and 4), which is consistent with an upward turbulent transport. The same conclusions apply for the profiles of the fluxes of variance $\overline{w'\theta_l'^2}$ and $\overline{w'q_w'^2}$ (Figs. 16 and 17), which have roughly the same shape as the variance profiles themselves (Figs. 5 and 6), with maxima in the trade inversion for $\overline{w'\theta_l'^2}$ and in the lower cloud levels for $\overline{w'q_w'^2}$. Finally, Figs. 18–21 show the third-order scalar correlations $\overline{\theta_l'^3}$, $\overline{\theta_l'^2 q_w'}$, $\overline{\theta_l' q_w'^2}$, $\overline{q_w'^3}$. Again, the agreement with the 3D data is better for θ_l than for q_w. The signs of these correlations are also of interest. Cumulus convection develops strong updrafts of cold and moist air relative to the environment, leading to positive $\overline{q_w'^3}$ and $\overline{\theta_l'^2 q_w'}$, and to negative $\overline{\theta_l'^3}$ and $\overline{\theta_l' q_w'^2}$. The $\overline{q_w'^3}$ profile shows a sharp minimum at the base of the clouds. Indeed, large negative values frequently are observed near the top of the mixed layer, as well as in numerical simulations of field experiments, due to the entrainment of drier air from the upper levels. The profile shown in Fig. 21 therefore is a compromise between this phenomenon and the development of the positively skewed distributions in the cumulus layer (see Part I) and in the lower mixed layer. This feature is well predicted by the 1D model.

6. Conclusion and future work

This extensive comparison between the 1D and 3D results shows that the models, having the same theoretical basis, are quite consistent with each other. However, they possibly have the same shortcoming as well, and a further comparison with field experimental results is needed. Whereas the 3D model simulates the turbulent movements, the 1D model only deals with averaged profiles of the mean quantities and turbulent correlations. Accordingly, it is roughly two orders of magnitude less expensive in computational power, and can therefore be of wider use. Clearly, some features are not satisfactorily described, and further improvements are needed. Turbulent transport is parameterized according to the quasi-Gaussian approximation, while the buoyancy production terms are expressed using a skewed exponential model for the probability densities. This inconsistency could possibly be the source of some spurious behavior. On the other hand, some theoretical work still has to be done to investigate the effect of the pressure correlations in the third-order moment equations.

The present study, nevertheless, suggests that the 1D model can be a powerful tool for research into the cloudy PBL, as it already has proven to be for the clear-sky case. Until now, most studies in pa-

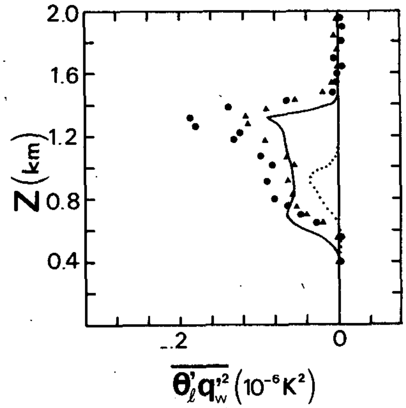

FIG. 20. As in Fig. 3 except the third-order correlation $\overline{\theta_l' q_w'^2}$.

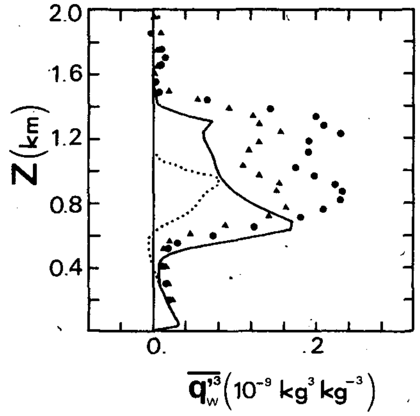

FIG. 21. As in Fig. 3 except the third-order moment of humidity.

rameterization of the trade-wind cumulus layer have been conducted with simple zero-order models. Although these models more or less depend on assumptions for the entrainment rate, they have been used (e.g., by Betts, 1973, 1976; Albrecht, 1979; Albrecht *et al.*, 1979), to acquire considerable understanding of the bulk structure of the trade-wind PBL, as well as of other types of cloudy PBL's. Hopefully, a higher order model such as the present one, will give further insight into the structure of the turbulent fluxes in such a layer, and will allow for a variety of parameterization studies. This model should, however, include an efficient interactive radiative scheme, and should be tested against a few different cases, obtained from 3D simulations under similar conditions. Of course, it would be even better to test the model using turbulence measurements through a cloud layer during a field experiment. This model further allows for the study of various types of cloudy PBL's, such as the layers of marine stratocumulus characteristic of cool coastal dry climates. For this purpose, only the mixing-length profile and the distribution law assumption inside the cloud layer may have to be revised. Similarly, the transition between these various regimes of the PBL can be studied as well. The proposed model therefore has potentially a wide range of applications.

Acknowledgments. This work is part of the author's unpublished "Thèse de 3è cycle". He would like to thank Drs. J. C. André and G. Sommeria for many stimulating discussions, as well as M. Coantic, G. De Moor, R. Du Vachat, and G. Therry for helpful comments. Extra acknowledgments are due to P. Lacarrère, for expertly drawing most of the figures.

REFERENCES

Albrecht, B. A., 1979: A model of the thermodynamic structure of the trade-wind boundary layer: Part II. Applications. *J. Atmos. Sci.*, **36**, 90–98.

——, A. K. Betts, W. H. Schubert and S. K. Cox, 1979: A model of the thermodynamic structure of the trade-wind boundary layer: Part I. Theoretical formulation and sensitivity tests. *J. Atmos. Sci.*, **36**, 90–98.

André, J. C., G. De Moor, P. Lacarrère, and R. Du Vachat, 1976a: Turbulence approximation for inhomogeneous flows. Part I: The clipping approximation. *J. Atmos. Sci.*, **33**, 476–481.

——, ——, —— and ——, 1976b: Turbulence approximation for inhomogeneous flows. Part II: The numerical simulation of a penetrative convection experiment. *J. Atmos. Sci.*, **33**, 482–491.

——, ——, ——, G. Therry and R. Du Vachat, 1978: Modeling the 24 h evolution of the mean and turbulent structures of the planetary boundary layer. *J. Atmos. Sci.*, **35**, 1861–1883.

——, P. Lacarrère and L. Mahrt, 1979: Sur la distribution verticale de l'humidité dans une couche limite convective. *J. Rech. Atmos.*, **13**, 135–146.

——, —— and K. Traoré, 1981: Pressure effects on triple correlations in turbulent convective flows. *Turbulent Shear Flows*, Vol. 3, Springer Verlag (to appear).

Betts, A. K., 1973: Nonprecipitating cumulus convection and its parameterization. *Quart. J. Roy. Meteor. Soc.*, **99**, 178–196.

——, 1976: Modeling subcloud layer structure and interaction with a shallow cumulus layer. *J. Atmos. Sci.*, **33**, 2363–2382.

Blackadar, A. K., 1962: The vertical distribution of wind and turbulent exchanges in neutral atmosphere. *J. Geophys. Res.*, **67**, 3095–3102.

Bougeault, Ph., 1981: Modeling the trade-wind cumulus boundary layer. Part I: Testing the ensemble cloud relations against numerical data. *J. Atmos. Sci.*, **38**, 2414–2428.

Businger, J. A., J. C. Wyngaard, Y. Izumi and E. F. Bradley, 1971: Flux-profile relationships in the atmospheric surface layer. *J. Atmos. Sci.*, **28**, 181–189.

Deardorff, J. W., 1974: Three-dimensional numerical study of turbulence in an entraining mixed layer. *Bound.-Layer Meteor.*, **7**, 199–226.

——, 1976: Usefulness of liquid-water potential temperature in a shallow cloud model. *J. Appl. Meteor.*, **15**, 98–102.

——, 1978: Closure of second- and third-moment rate equations for diffusion in homogeneous turbulence. *Phys. Fluids*, **21**, 525–530.

Launder, B. E., 1975: On the effects of a gravitational field on the turbulent transport of heat and momentum. *J. Fluid Mech.*, **67**, 569–581.

LeMone, M. A., and W. T. Pennell, 1976: The relationship of trade-wind cumulus distribution to subcloud layer fluxes and structure. *Mon. Wea. Rev.*, **104**, 524–539.

Lenschow, D. H., 1970: Airplane measurements of planetary boundary layer structure. *J. Appl. Meteor.*, **9**, 874–884.

Lilly, D. K., 1968: Models of cloud-topped mixed layers under a strong inversion. *Quart. J. Roy. Meteor. Soc.*, **94**, 292–309.

Manton, M. J., 1979: On the prediction of infra-red cooling rates in the clouds with variable properties. *J. Rech. Atmos.*, **13**, 93–110.

Mellor, G. L., 1977: The Gaussian cloud model relations. *J. Atmos. Sci.*, **34**, 356–358 and 1483–1484.

Oliver, D. A., W. S. Lewellen and G. G. Williamson, 1978: The interaction between turbulent and radiative transport in the development of fog and low-level stratus. *J. Atmos. Sci.*, **35**, 301–316.

Pennell, W. T., and M. A. LeMone, 1974: An experimental study of turbulence structure in the fair weather trade-wind boundary layer. *J. Atmos. Sci.*, **31**, 1308–1323.

Randall, D. A., 1980: Entrainment in a stratocumulus layer with distributed radiative cooling. *J. Atmos. Sci.*, **37**, 148–159.

Sommeria, G., 1976: Three dimensional simulation of turbulent processes in an undisturbed trade wind boundary layer. *J. Atmos. Sci.*, **33**, 216–241.

——, and J. W. Deardorff, 1977: Subgrid scale condensation in models of non-precipitating clouds. *J. Atmos. Sci.*, **34**, 345–355.

——, and M. A. LeMone, 1978: Direct testing of a three dimensional model of the planetary boundary layer against experimental data. *J. Atmos. Sci.*, **35**, 25–39.

Veyre, Ph., G. Sommeria and Y. Fouquart, 1980: Modèlisation de l'effet des hétérogénéités du champ radiatif infra-rouge sur la dynamique des nuages. *J. Rech. Atmos.*, **14**, 89–108.

Wyngaard, J. C., and O. R. Coté, 1974: The evolution of a convective planetary boundary layer: A higher-order closure model study. *Bound.-Layer Meteor.*, **7**, 289–308.

——, W. T. Pennell, D. H. Lenschow and M. A. LeMone, 1978: The temperature humidity covariance budget in the convective boundary layer. *J. Atmos. Sci.*, **35**, 47–58.

Yamada, T., and G. L. Mellor, 1979: Anumerical simulation of BOMEX data using a turbulence closure model coupled with ensemble cloud relations. *Quart. J. Roy. Meteor. Soc.*, **105**, 915–944.